

Interaction of H₂O with the Platinum Pt (001), (011), and (111) Surfaces: A Density Functional Theory Study with Long-Range Dispersion Corrections

Marietjie J. Ungerer,^{†,‡,§} David Santos-Carballal,^{‡,§} Abdelaziz Cadi-Essadek,[‡] Cornelia G. C. E. van Sittert,^{*,†,§} and Nora H. de Leeuw^{*,‡,§}

[†]Laboratory for Applied Molecular Modelling, Research Focus Area: Chemical Resource Beneficiation, North-West University, Private Bag X6001, Potchefstroom 2520, South Africa

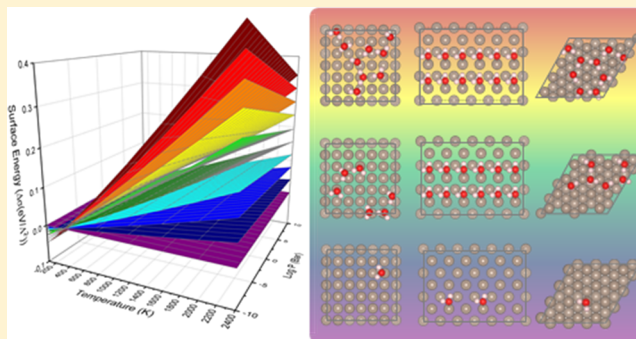
[‡]School of Chemistry, Cardiff University, Main Building, Park Place, Cardiff CF10 3AT, United Kingdom

[§]Materials Modelling Centre, School of Physical and Mineral Sciences, University of Limpopo, Private Bag X1106, Sovenga 0727, South Africa

[#]Department of Earth Sciences, Utrecht University, Princetonplein 8A, 3584 CD Utrecht, The Netherlands

S Supporting Information

ABSTRACT: Platinum is a noble metal that is widely used for the electrocatalytic production of hydrogen, but the surface reactivity of platinum toward water is not yet fully understood, even though the effect of water adsorption on the surface free energy of Pt is important in the interpretation of the morphology and catalytic properties of this metal. In this study, we have carried out density functional theory calculations with long-range dispersion corrections [DFT-D3-(BJ)] to investigate the interaction of H₂O with the Pt (001), (011), and (111) surfaces. During the adsorption of a single H₂O molecule on various Pt surfaces, it was found that the lowest adsorption energy (E_{ads}) was obtained for the dissociative adsorption of H₂O on the (001) surface, followed by the (011) and (111) surfaces. When the surface coverage was increased up to a monolayer, we noted an increase in $E_{\text{ads}}/\text{H}_2\text{O}$ with increasing coverage for the (001) surface, while for the (011) and (111) surfaces, $E_{\text{ads}}/\text{H}_2\text{O}$ decreased. Considering experimental conditions, we observed that the highest coverage was obtained on the (011) surface, followed by the (111) and (001) surfaces. However, with an increase in temperature, the surface coverage decreased on all the surfaces. Total desorption occurred at temperatures higher than 400 K for the (011) and (111) surfaces, but above 850 K for the (001) surface. From the morphology analysis of the Pt nanoparticle, we noted that, when the temperature increased, only the electrocatalytically active (111) surface remained.



1. INTRODUCTION

Increasingly, global research is focusing on clean, renewable, and sustainable energy production. Some of the more promising alternative methods for the production of energy include wind,^{1,2} solar,^{3,4} hydroelectricity,^{5–7} or combinations thereof.^{8–13} Another potentially viable energy source is hydrogen (H₂), which is an ideal energy carrier for a variety of fuel cell applications, including in stationary, mobile, and portable power applications.¹⁴

H₂ gas can be produced via a number of technologies, including from carbon-based fuels¹⁵ or from renewable sources such as biomass¹⁶ and water.^{17,18} Among the different routes to the production of H₂, the non-carbon-based hybrid sulfur (HyS) cycle has shown itself as a promising, potentially large-scale process.^{19,20} In this process, the net reaction is the splitting of water into H₂ and O₂ via the electro-oxidation of

SO₂/H₂SO₄. In this system, various anode catalysts have been tested,²⁰ and metallic platinum (Pt) consistently showed both high activity and stability,^{13,21,22} especially when it was supported on carbon particles. Moreover, Pt is already used as a catalyst²³ in a wide variety of reactions, where water acts as a reactant or spectator, influencing the behavior of the surface.²⁴

Water has a complex structure; when monolayers are adsorbed on a surface, it does not only form two-dimensional structures, but it can also create three-dimensional structures resembling bulk liquid water.²⁵ Both computational and experimental works have shown that water molecules on a

Received: June 27, 2019

Revised: September 25, 2019

Published: September 25, 2019

metal surface are arranged in several layers interacting through an extensive hydrogen-bond network.^{26,27} It is therefore important in computational studies that appropriate long-range dispersion interactions are included in the calculations to describe accurately the water–metal interface,^{28,29} for example, by employing density functional theory (DFT) methods with van der Waals corrections.^{30,31} Another challenge in modeling the adsorption of water on a metallic surface is the high fluctuations in the atomic positions in a liquid, which requires the inclusion of several different configurations^{32,33} in the initial computational setup. It has been shown^{34,35} that the most reliable computational results are not necessarily obtained via the addition of more waters to a surface but, more importantly, by considering the way the water molecules interact with each other through the creation of hydrogen bonds and higher-order structures, including hexamers, heptamers, and octamers. However, the detailed description of the binding of water molecules onto Pt surfaces is still not complete, even though it is important for the improvement of the catalytic properties of the Pt material that we understand the fundamental reaction processes that take place on the Pt catalytic surface. The starting point here will be an in-depth understanding of the interactions between the water molecules and the metal surface atoms.

In this paper, we have used DFT calculations to predict the interaction of water with the Pt (001), (011), and (111) surfaces. We examine the electronic properties of the system, including simulated scanning tunneling microscopy (STM) images, the work function, and local densities of states. Surface phase diagrams have also been generated through consideration of the surface free energies and water chemical potential to determine the effects of temperature and pressure on the surface coverage. The aim of our study was the development of a comprehensive understanding of the water–surface chemistry, including adsorption and desorption and the effect of water on the electrocatalytically active surfaces of platinum metal.

2. COMPUTATIONAL METHODS

2.1. Calculation Details. The Vienna Ab Initio Simulation Package (VASP)^{36–39} was used to simulate the Pt surfaces and their interactions with water. The projector augmented wave (PAW)^{40,41} potential was employed to describe the interaction between the valence and the core electrons. The core electrons of Pt and O were defined up to and including the 5p and 1s orbitals, respectively. For the H atoms, all the electrons were treated as valence electrons. The Perdew, Burke, and Ernzerhof (PBE)^{42,43} functional within the generalized gradient approximation (GGA) was applied in all calculations. Plane waves were included to a cutoff of 400 eV. The Methfessel–Paxton scheme order 1⁴⁵ was used with a smearing of 0.05 eV to determine the partial occupancies during geometry optimization, ensuring an electronic entropy of less than 1 meV·atom^{−1}. However, the tetrahedron method with Blöchl corrections⁴⁶ was used in the final static simulations to obtain accurate total energies, charges, and density of states. The electronic and ionic optimization criteria were 10^{−5} eV and 10^{−2} eV·Å^{−1}, respectively, and the conjugate gradient technique was adopted for the geometry optimizations.

Pt has an *Fm3m* crystal structure.⁴⁷ The bulk Pt structure was calculated within a primitive face-centered cubic (fcc) cell using a Γ -centered 17 × 17 × 17 Monkhorst-Pack⁴⁸ *k*-point mesh. Our calculated fcc Pt lattice constant was 3.926 Å, in

excellent agreement with the experimental value of 3.924 Å.^{49,50}

The Pt (001), (011), and (111) surfaces were investigated by simulating the periodic p(3 × 3), p(3 × 3), and p(4 × 4) supercells, respectively, which were generated from the bulk using the METADISE code.⁵¹ Vacuum of 15 Å, in the *z* direction, was added to avoid interaction between the neighboring cells. Four atomic layers were considered for the slabs, and the surface areas of the supercells were 138.17, 196.18, and 106.79 Å² for the (001), (011), and (111) surfaces, respectively. The atoms in the two bottom layers of the supercell were fixed in the calculated bulk locations, and the atoms in the remaining two layers were allowed to relax. A Γ -centered 7 × 7 × 1 Monkhorst-Pack *k*-point grid was used in all the surfaces to sample the Brillouin zone.

The unrelaxed (γ_u) and relaxed (γ_r) surface energies were determined using eqs 1 and 2, respectively

$$\gamma_u = \frac{E_{\text{slab},u} - N_{\text{Pt,slab}} E_{\text{Pt,bulk}}}{2A_{\text{slab}}} \quad (1)$$

$$\gamma_r = \frac{E_{\text{slab},r} - N_{\text{Pt,slab}} E_{\text{Pt,bulk}}}{A_{\text{slab}}} - \gamma_u \quad (2)$$

where $E_{\text{slab},u}$, $E_{\text{slab},r}$, and $E_{\text{Pt,bulk}}$ are the energies of the unrelaxed slab, the half-relaxed slab, and the bulk, respectively. $N_{\text{Pt,slab}}$ and A_{slab} represent the number of Pt atoms in the slab and the surface area of the slab, respectively. The percentage of relaxation (*R*) was calculated as the difference between the unrelaxed and relaxed surface energies, divided by the unrelaxed surface energy, multiplied by 100.

Atomic charges were obtained using the Bader analysis,^{52–55} which partitions space into nonspherical atomic regions enclosed by local minima in the charge density. The Tersoff–Hamann⁵⁶ approach was used to simulate scanning tunneling microscopy (STM) images. In this approach, the tunneling current is proportional to the local density of states (LDOS) of the surface at the position of the tip integrated between the Fermi level and the applied bias. The STM images were mapped in terms of the height as a function of the tip position over the surface using the HIVE⁵⁷ program.

The isolated H₂O molecule was modeled in a periodic box of 12 × 13 × 14 Å³ to ensure negligible interaction with its images of neighboring cells. The Gaussian smearing scheme⁴⁵ was used during geometry optimization and energy calculations with a smearing of 0.05 eV. A Γ -centered 1 × 1 × 1 Monkhorst-Pack⁴⁸ *k*-point mesh was also used. Dipole corrections were added in all directions, and the H₂O molecule was computed without symmetry.

2.2. Coverage-Dependent Surface Energies. The average adsorption energy E_{ads} per water molecule on the Pt surface was calculated as follows⁵⁸

$$E_{\text{ads}} = \frac{1}{N_w} [E_{\text{slab},r}^{N_w \neq 0} - (E_{\text{slab},r}^{N_w = 0} + N_w E_w)] \quad (3)$$

where $E_{\text{slab},r}^{N_w \neq 0}$, $E_{\text{slab},r}^{N_w = 0}$, and E_w are the energies of the slab with the water molecules adsorbed, the clean surface, and the isolated water molecule, respectively. N_w corresponds to the number of adsorbed water molecules.

To determine the thermodynamics of different H₂O coverages on Pt (001), (011), and (111) surfaces, the surface free energy (σ) is calculated for different temperatures (*T*) and

H₂O chemical potential (μ_w). The resulting change in surface free energy upon H₂O adsorption is denoted as

$$\Delta\sigma(T, p) = \frac{1}{A_{\text{slab}}} [E_{\text{slab},r}^{N_w \neq 0} - E_{\text{slab},r}^{N_w = 0} - N_w \cdot \mu_w] \quad (4)$$

Surface coverage (θ) represents the number of adsorbed water molecules (N_w) divided by the total number of adsorption sites (N) as

$$\theta = \frac{N_w}{N} \quad (5)$$

$\theta = 0$ indicates that no adsorption has taken place, while $\theta = 1$ shows that adsorption has reached a monolayer.

The chemical potential of molecular H₂O in the gas phase can also be expressed as

$$\mu_w(T, p) = E_w + \Delta G_w(T, p_0) + k_B T \ln \frac{p}{p_0} \quad (6)$$

where E_w is the DFT energy of the H₂O molecule, $\Delta G_w(T, p_0)$ is the Gibbs free energy difference per H₂O molecule between 0 K and T at $p_0 = 1$ bar, which has been extracted from thermodynamic tables.⁵⁹ The last term ($k_B T \ln \frac{p}{p_0}$) denotes the

free energy change of H₂O gas at constant temperature (T) when the partial pressure changes from p_0 to p . To express the chemical potential, independent of the calculated quantities, the energy of water was omitted from eq 6 and added to eq 4.

To determine the effect of H₂O adsorption on the Pt (001), (011), and (111) surfaces, Wulff morphologies⁶⁰ were constructed using the GDIS program.⁶¹ The equilibrium Wulff crystal is constructed, assuming that the distance of the crystal face (d_{001} , d_{011} , d_{111}) to the center of the nanoparticle is proportional to their surface free energies as

$$\frac{d_{001}}{\sigma_{001}} = \frac{d_{011}}{\sigma_{011}} = \frac{d_{111}}{\sigma_{111}} \quad (7)$$

3. RESULTS AND DISCUSSION

3.1. Surface Structures. Figure 1 shows the side and top views of the Pt (001), (011), and (111) surfaces as constructed for our simulations. All three surfaces are planar, bulk-terminated structures, with four layers in each slab. All three surfaces were nonpolar, with the Pt (001) being a smooth surface, Pt (011) being atomically rough and forming channels on the surface, and Pt (111) again being smooth with an fcc arrangement. It has been shown that long-range dispersion approximations influence not only the lattice parameters of a modeled surface, but also the surface energy of the surface.⁶² To optimize the geometry of the Pt (001), (011), and (111) surfaces, three different long-range dispersion approximations were tested, including (i) without dispersion interactions (DFT), (ii) the DFT-D2 method of Grimme,⁶³ (iii) the zero damping DFT-D3 method of Grimme,⁶⁴ and (iv) the DFT-D3 method with Becke–Johnson damping.⁴⁴

Table 1 shows the lattice parameters, relaxed and unrelaxed surface energies, and the surface areas for the Pt (001), (011), and (111) surfaces, as determined using the different long-range dispersion correction approximations. From the lattice parameters, it was seen that the best correlation was obtained using the DFT-D3(BJ) method, followed by the DFT-D3, DFT, and DFT-D2 methods. The experimental lattice parameter of Pt is 3.925 Å,⁶⁵ which was overestimated by

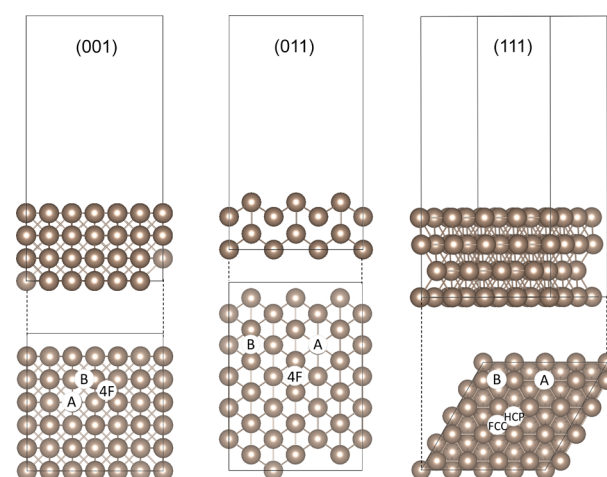


Figure 1. Side and top views of the Pt (001), (011), and (111) surfaces. The symmetrically inequivalent adsorption sites for H₂O are indicated, that is, fourfold hollow (4F), bridge (B), atop (A), face-cubic centered (fcc), and hexagonal close packed (hcp) sites. The gold color is used throughout this paper for Pt.

0.03 and 1.1% by the DFT-D3(BJ) and standard DFT methods, while with DFT-D3 and DFT-D2, it was underestimated by 0.2 and 2.1%, respectively. In terms of surface energy, all methods followed the same trend where Pt (111) has the lowest surface energy, followed by the (001) and (011) surfaces. An experimental surface energy of 2.48 J/m² has been reported in the literature,⁶⁶ and compared to this prior investigation, the DFT method underestimates the energies by 48, 37, and 65% for the Pt (001), (011), and (111) surfaces, respectively, while DFT-D2 overestimates the energies for all three surfaces by 68, 78, and 60%, respectively. The best correlation for surface energies was with DFT-D3 and DFT-D3(BJ) methods, both of which have less than 18% deviation for all the surfaces with respect to the experiment, which also correlated with the literature.⁶⁷

A number of calculations were benchmarked using the opt-PBE self-consistent van der Waals functional^{29,68} and found the lattice parameter of 3.841 Å, which compares to the DFT-D2 method. Furthermore, the unrelaxed (γ_u) and relaxed (γ_r) surface energies were underestimated at 1.633 and 1.603 J/m², respectively, when compared to 2.17 eV obtained with the modified embedded-atom method.⁶⁹

Taking all of the data into consideration, the DFT-D3(BJ) setting gave the best agreement with the experimental lattice parameter, but a range of different values for the surface energy have been reported. Comparing the surface energy determined with the different methods for the three surfaces to the experimental value of 2.49 J/m²,⁷² it can be seen that the DFT-D3(BJ) method gave the best agreement and was therefore used in the determination of the surface properties and adsorption energies in the following sections.

The work function, a descriptor inversely related to chemical reactivity, was calculated for the pristine Pt (001), (011), and (111) surfaces (Table 1), where it was determined that removing an electron would be the easiest from the (001) surface, followed by the (111) and (011) surfaces. The literature also reports this tendency,⁷⁰ with the lowest work function for the (011) surface, followed by (001) and (111) surfaces, which were, however, dependent on the surface area and modeling approximation used. The work function alone

Table 1. Lattice Parameters (a) for the Bulk Pt System, Unrelaxed (γ_u) and Relaxed (γ_r) Surface Energies, Percentage of Relaxation (R) and the Surface Areas (A) for the Pt (001), (011) and (111) Surfaces Calculated with Several Long-Range Dispersion Correction Methods^a

surface	parameter	DFT	DFT-D2	DFT-D3	DFT-D3(BJ)	other works
Pt (001)	a (Å)	3.968	3.841	3.918	3.926	3.924 ^{49,50}
	γ_u (J/m ²)	1.327	4.170	2.580	2.472	
	γ_r (J/m ²)	1.294	4.166	2.575	2.462	1.81, ⁷⁰ 2.17 ⁶⁹
	R (%)	2.48	0.09	0.23	0.40	
	A (Å ²)	141.68	132.76	138.17	138.72	
	Φ (eV)				5.89	5.66 ⁷⁰
Pt (011)	d-band center (eV)				−2.24	
	γ_u (J/m ²)	1.639	4.461	2.789	2.691	
	γ_r (J/m ²)	1.557	4.407	2.710	2.615	1.85, ⁷⁰ 2.37 ⁷¹
	R (%)	5.03	1.22	2.83	2.83	
	A (Å ²)	200.36	125.16	195.40	196.18	
	Φ (eV)				5.49	5.26 ⁷⁰
Pt (111)	d-band center (eV)				−2.00	
	γ_u (J/m ²)	0.871	3.961	2.209	2.055	
	γ_r (J/m ²)	0.866	3.961	2.193	2.046	1.49, ⁷⁰ 2.49 ⁷²
	R (%)	0.62	1.05	0.72	0.43	
	A (Å ²)	109.07	102.20	106.36	106.79	
	Φ (eV)				5.64	5.69 ⁷⁰
	d-band center (eV)				−2.44	−2.45 ⁷³

^aThe work function (Φ) and d-band center values for these surfaces were only calculated using the DFT-D3(BJ) method.

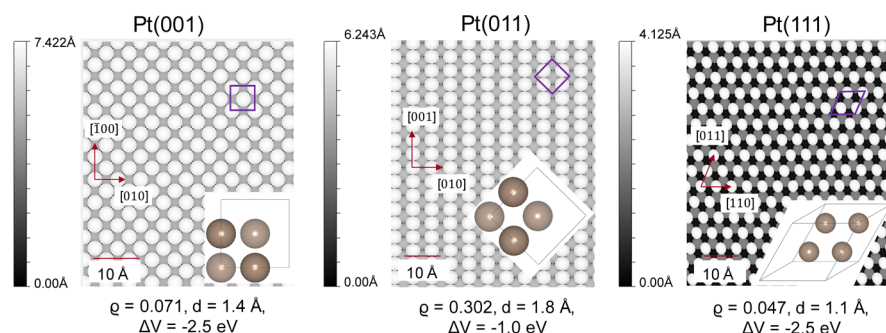


Figure 2. Simulated STM images of the Pt (001), (011), and (111) surfaces. The density (ρ), tip distance (d), and bias (ΔV) are also indicated.

cannot be used to predict reactivity though as it is dependent on the surface properties, as well as the temperature.⁷⁴

The positions of the d-band center have been used before to explain adsorption tendencies on transition metal surfaces.⁷⁵ The general trend is that the higher in energy the occupied d-states, the stronger the bond with a molecule that accepts electrons from the metal. Among the three surfaces, it was calculated (Table 1) that the Pt (111) surface had the highest d-band center energy, followed by the (001) and (011) surfaces. We found that our calculated d-band center for the Pt (111) surface is in excellent agreement with the value of −2.45 eV reported by Xin et al.⁷³

STM images were simulated for the optimized Pt surfaces and derived from the spatial distribution of the valence band states in the vicinity of the Fermi level (E_F). Figure 2 shows our STM images for the Pt (001), (011), and (111) surfaces. For Pt (001), a checker board-like structure can be seen, which is similar to the pattern reported for Cu(100)⁷⁶ and Ag(100).⁷⁷ For Pt (011), the grooves formed in the [001] direction on the surface are evident, with every second row higher in the surface shown in a darker color, which means that they are closer to the scanning tip. The alternating rows in the [010] direction are lower and therefore in a lighter gray color.

This missing row arrangement was also reported by Feenstra and Hla⁷⁸ for the isostructural fcc Au (110) surface. The STM image of the Pt (111) shows the honeycomb structure of Pt, as reported in previous experimental findings.⁷⁹ As these are all pristine surfaces, no deformations or reconstructions were observed.

3.2. Single H₂O Molecule Adsorption. Figure 1 shows the side and top views of the Pt (001), (011), and (111) surfaces, where we have indicated all the possible unique adsorption sites for H₂O. The (001) and (011) surfaces have fourfold hollow (4F), bridge (B), and atop (A) sites, while the (111) surface has bridge (B), top (T), face-centered cubic (fcc), and hexagonal close-packed (hcp) sites. Three different adsorption modes⁸⁰ were investigated on each surface, one where the H₂O molecule is parallel to the Pt surface and all three atoms could interact with the surface, the second where one H was turned upward and only the OH could interact with the surface, and the third where one of the H atoms was turned downward to interact with the Pt surface. All three adsorption modes were investigated for each adsorption site shown in Figure 1.

Water on metal surfaces is usually believed to be intact, except when coadsorbed with other molecules or atoms.^{82,83}

However, a recent DFT study has suggested that a water bilayer on Ru (0001) is half-dissociated, with one O–H bond broken in the dissociated water molecules.⁸⁴ In another study of water bilayers on Pt, up to 9% of the H₂O molecules dissociated.³⁴ Even though it would be less likely to have a single molecule of water dissociate on the surface, it was still decided to include the (001)_{diss} data for both single adsorption and higher surface coverage. For reasons of comparison, it was also decided to include the most stable dissociation configurations on both the (011) and (111) surfaces. The most stable structures found for the adsorption of the water monomer on top of the Pt surfaces are shown in Figure 3, with the bond distances and angles of the adsorbed H₂O with respect to the Pt surfaces listed in Table 2.

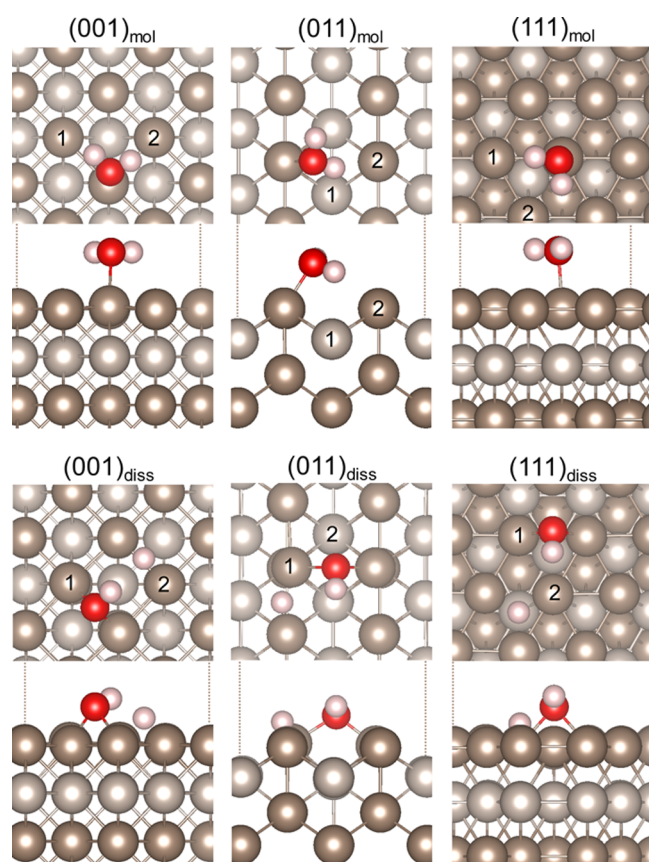


Figure 3. Lowest energy adsorption sites of H₂O on Pt (001), (011), and (111) surfaces. Pt (001)_{diss} and Pt (001)_{mol} indicate the adsorption of dissociated and molecular H₂O, respectively. The atom colors red, white, and gold denote oxygen, hydrogen, and platinum atoms, respectively. The lighter gold color is used to distinguish between the platinum atoms of different layers.

On the (001) surface, two very different configurations released the largest adsorption energies, that is, dissociated and molecular H₂O, which will be denoted as (001)_{diss} and (001)_{mol}, respectively. In the case of (001)_{diss}, the OH group and dissociated H atom sat in the bridge hollow site, with the O–Pt distance at 2.096 Å, hydroxy H–Pt1 distance at 2.531 Å, and hydroxy H–Pt2 distance at 2.956 Å. The H–Pt2 distance for the dissociated H was 1.754 Å. When associatively adsorbed on Pt (001)_{mol}, the H₂O molecule laid parallel to the Pt surface with the H atoms directed toward the bridge hollow position, where the O–Pt distance was 2.311 Å and the

H–Pt distances were 2.831 and 2.786 Å for Pt1 and Pt2 (Figure 3), respectively. The H–O–H angle correlated with experimental values at 104.48°, suggesting that the water was physisorbed.

On the (011) surface, one of the hydrogens of H₂O is pointing along the direction of the ridge it is adsorbed to, whereas the other H points toward the neighboring ridge, as can be seen in Figure 3. The O–Pt distances on the (011) surface are slightly shorter than on the other surfaces, although the H–O–H angle differs by less than 1° from the calculated value for Pt (001). In the dissociated system Pt (011)_{diss}, the OH group is bound at the oxygen to the surrounding Pt atoms on the neighboring ridges, following the direction of the valley. The dissociated H atom is bound in a bridge position between two Pt atoms on the ridge, which was also found by Shi and Sun.⁸⁵

Similar to the Pt (001)_{mol} adsorption, on the (111) surface, the H₂O molecule adsorbs flat, with one H atom directed toward a surface Pt (Pt1) and the other in the direction of an fcc Pt (Pt2) (Figure 3). Carrasco and co-workers³⁰ also showed that the most stable single H₂O molecule adsorption was parallel atop the Pt atom. In this work, the O–Pt distance was calculated at 2.386 Å, and the H–O–H angle was calculated at 104.94°, while in the literature, the O–Pt distance was reported as between 2.49 and 2.82 Å, depending on the type of dispersion correction method used in the calculations.³⁰ Similar to our work on the pristine surfaces, Carrasco and co-workers³⁰ have found that, when either no dispersion correction, opt-PBE, or opt-B88²⁹ was added, the O–Pt distance correlated with our work, but when revPBE was used, it was overestimated by 15%. The DFT-D3(BJ)^{44,64} method we have used is geometry-dependent and therefore accounts for the coordination number of the adsorbed atoms. Our simulations suggest that water may bind more strongly to the Pt (111) surface than was found previously.³⁰ Similar to the (001)_{diss} and (011)_{diss} systems, adsorption of the dissociated H₂O on the (111) surface showed that the OH group is in the bridge position, where the oxygen is bound to two neighboring Pt atoms. The dissociated hydrogen was in a neighboring fcc hollow site, which was also reported as energetically the most stable adsorption manner of hydrogen on the Pt (111) surface by Shi and Sun.⁸⁵

The adsorption energy for a single water molecule, $N_w = 1$, was calculated to be much larger on the (001) surface than the (011) and (111) surfaces, indicating that adsorption and dissociation are favored on the (001) surface. Carrasco and co-workers³⁰ reported monomer adsorption energies for the Pt (111) surface between –0.24 and –0.40 eV, again depending on the dispersion correction approximation chosen. These values are in fair agreement with our adsorption energy calculated for the (111) surface, again indicating somewhat stronger binding in this study compared to the literature.³⁰ Comparing the adsorption energy of the dissociated water on all the surfaces, it can be seen that it was energetically favored on the (001) surface, followed by the (111) and (011) surfaces. As part of the opt-PBE benchmarking, for the adsorption of both molecular and dissociative adsorption of H₂O, we found the values to be slightly endothermic at 0.108 and 0.098 eV, respectively, which differed by more than 0.5 eV from reported values.³⁰

Table 2 lists the simulated wavenumbers of the fundamental vibrational modes of the adsorbed H₂O molecule on the (001), (011), and (111) surfaces, which include the asymmetric

Table 2. Adsorption Energy (E_{ads}), Bond Distance (d), and Angles (\angle) as well as the Simulated Wavenumbers (cm^{-1}) of the Fundamental Vibrational Modes of the Adsorbed H_2O Molecule on the Pt (001), (011), and (111) Surfaces^a

parameter	(001) _{diss}	(001) _{mol}	(011) _{diss}	(011) _{mol}	(111) _{diss}	(111) _{mol}	literature
E_{ads} (eV)	−1.758	−1.675	−0.258	−0.699	−0.380	−0.464	
d (Å)							
O–Pt	2.096	2.311	2.225	2.240	2.169	2.386	
H–Pt1	2.531	2.831	2.619	3.050	2.591	2.973	
H–Pt2	2.956, 1.754	2.786	3.292, 1.714	2.430	3.317, 1.873	3.164	
\angle (°)							
H–O–H		104.55		103.76		104.94	104.48 ^b
Pt–O–H	104.55	97.94	102.51	99.40	104.14	97.72	
ν_{asym} (cm^{-1})	3558	3617		3620	3572	3684	3756 ^c , 3727 ^d
ν_{sym} (cm^{-1})		3521		3178		3574	3657 ^c , 3613 ^d
δ (cm^{-1})	1365	1547		1524	1118	1553	1595 ^c , 1552 ^d
Δq (e)	−0.393	0.109	−0.458	0.095	−0.338	0.087	

^aThe presented vibrational modes are the asymmetric stretching (ν_{asym}), symmetric stretching (ν_{sym}), and bending (δ) modes. Charge transfer (Δq) for H_2O adsorption on the different Pt surfaces is also given. ^bExperimental value. ^cExperimental frequency values. ^dOther modeled vibrational data.⁸⁷

stretching (ν_{asym}), symmetric stretching (ν_{sym}), and bending (δ) vibrational modes. For completeness, the data for the dissociated H_2O adsorptions were also included. For the dissociated H_2O , we can only report the OH stretching at 3558 cm^{-1} , which falls within 100 cm^{-1} for the stretching and bending modes, when we compare our vibrational results with experimentally measured values.⁸⁶ Comparing our results with modeled vibrational data, these were again within 60 cm^{-1} for the single H_2O molecule on Pt (111).⁸⁷ Due to the way the dissociated H_2O adsorbed onto the (011) surface, no OH stretching could be calculated.

From the charge analysis in Table 2, in the case of the dissociated H_2O , it was observed that electrons between 0.3 and 0.5 e^- were transferred from the Pt surfaces to the molecule, whereas in the adsorption of H_2O on all three surfaces, the molecule provided $\sim 0.1 \text{ e}^-$ to the Pt surface. Figure 4 shows the isosurfaces of the electron density difference between H_2O and the Pt surfaces, which was calculated by subtracting the electron density of a pristine Pt surface and that of a single H_2O molecule from the total electron density of the modeled system using the same geometries. Yellow and blue represent positive (electron-depleted) and negative (electron-gained) electron densities, respectively. As expected, in the (001)_{diss} system, the dissociated H atom was electron-depleted ($\Delta q = 0.623 \text{ e}^-$) relative to the surrounding Pt atoms, whereas the OH part followed a more complex pattern. However, from the Bader charge of each atom, it was seen that the OH group, as a whole, gained electrons ($\Delta q = -1.016 \text{ e}^-$). Dissociation on the (111) surface showed similar results, where H was electron-depleted ($\Delta q = 0.639 \text{ e}^-$) and the OH group gained electrons ($\Delta q = -0.977 \text{ e}^-$). However, even though the (011) surface follows the same trend, the values differ, with H becoming more electron-depleted ($\Delta q = 1.000 \text{ e}^-$) and OH gaining nearly another 50% more electron density ($\Delta q = -1.458 \text{ e}^-$). In contrast, for molecular adsorption, that is, the (001), (011), and (111) systems, electrons were donated from the molecule to the surface, and as also suggested by the positive Δq values from Table 2, the adsorption energies followed the same trend as the charge transfer values.

3.3. H_2O Surface Coverage. To consider the effect of surface coverage, the number of adsorbed H_2O molecules (N_{w}) was increased until a monolayer was obtained on all Pt

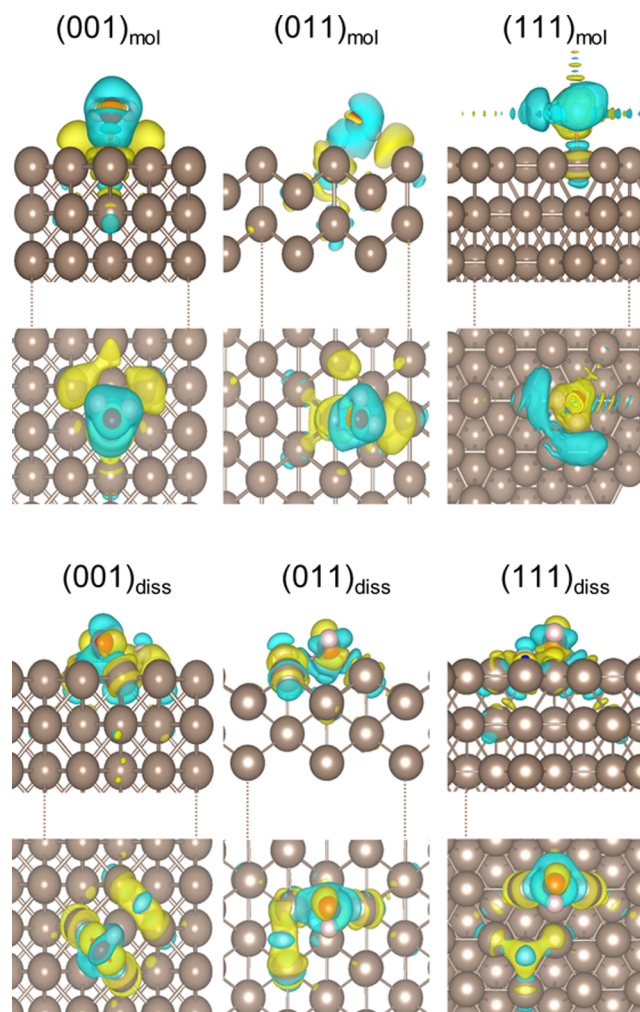


Figure 4. Isosurfaces of the electron density difference between H_2O and Pt (001), (011), and (111), both for the molecular and dissociative adsorbed systems. Yellow and blue represent positive (electron-gained) and negative (electron-depleted) electron densities with ± 0.00098 , ± 0.00101 , and $\pm 0.00252 \text{ e}/\text{\AA}^3$ for the molecular isosurfaces and ± 0.00255 , ± 0.00239 , and $\pm 0.00276 \text{ e}/\text{\AA}^3$ for the dissociative isosurfaces, respectively, for Pt (001), (011), and (111).

surfaces. The lowest energy configurations for single H_2O adsorption were used as the initial geometries for the increasing surface coverages. More than 30 configurations for each surface and at different coverages were considered, with the lowest energy configurations shown below. Figure 5 shows

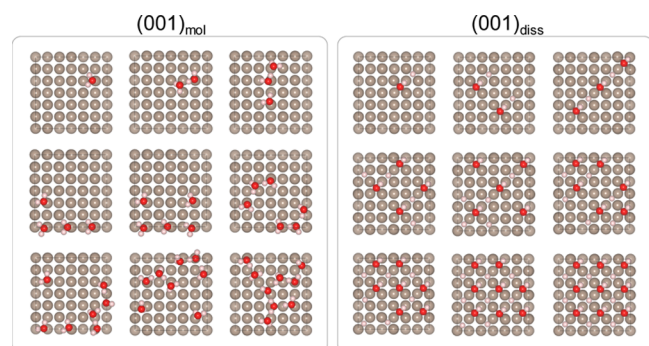


Figure 5. Molecularly and dissociatively adsorbed H_2O coverage on the Pt (001) surface.

the geometries of water molecules with increasing coverages of molecularly adsorbed H_2O until full coverage was reached. As the concentration increased, the adsorbed H_2O molecules tend to form hexagonal rings when the metal surface allows, as could be expected from the hexagonal structure of water ice I as a result of donor and acceptor hydrogen bonding between water molecules. As already mentioned, owing to the observation of water dissociation on the Pt surface, we considered that it would be interesting to see how H_2O would behave in its dissociated state when a surface is fully covered, as shown in Figure 5. However, as the surface coverage increased, the mode of adsorption remained the same; no further dissociation or recombination occurred during the geometry optimizations.

Similarly, it was seen on the (011) surface in Figure 6 that the adsorption manner of H_2O did not change as the surface coverage increased. Hydrogen bonds formed between every successive H_2O , leading to the formation of water strands in the channels of the (011) surface.

Figure 7 shows the surface coverage on the (111) surface. Compared to the other surfaces, the mode of adsorption changed the most, explaining the formation of penta- or hexagonal rings on the surface. For all the Pt surfaces, it was seen that, if the subsequent H_2O molecules were situated more than one adsorption site away from each other, then the adsorption geometry stayed the same as for the single molecule, suggesting that they behave as isolated adsorbates. However, if the adsorption sites were next to each other, then the geometry changed: the OH fragment would be parallel to the surface with the second H either pointing toward or away from the surface. At higher coverages ($\theta > 0.5$), the H_2O molecules formed hexagonal rings on the surfaces, as reported previously in the literature.^{33,88,89} More hydrogen bonds between the H_2O molecules also lead to larger average adsorption energies.

Figure 8 shows the calculated average adsorption energy as a function of the surface coverage of H_2O . For Pt (001)_{diss}, the value of E_{ads} per water molecule decreased with N_w , which indicates that, although adsorption energies per water molecule remain negative, initial adsorption of isolated water was more favorable than higher coverages. In the case of molecular H_2O adsorption Pt (001)_{mol}, E_{ads} decreased with N_w up to 50%

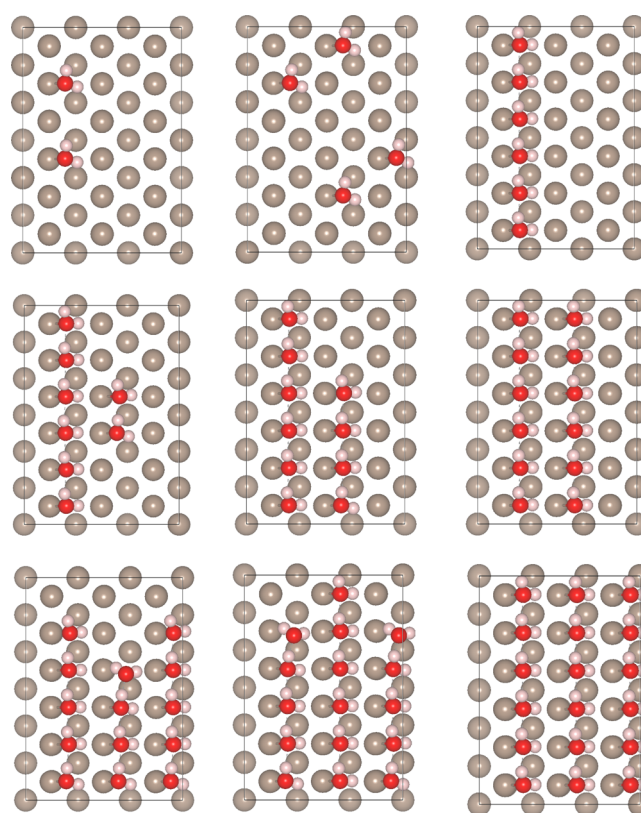


Figure 6. Molecularly adsorbed H_2O coverage on the Pt (011) surface.

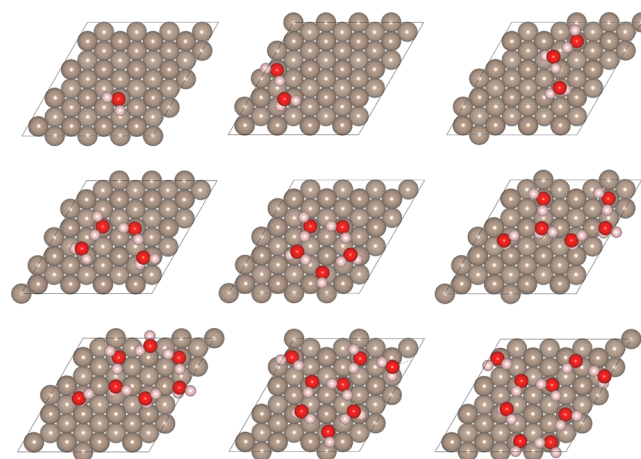


Figure 7. Molecularly adsorbed H_2O coverage on the Pt (111) surface.

surface coverage, after which the adsorption energy stabilized around -0.8 eV/ H_2O . This trend indicates that this surface has a high affinity to adsorb one to four H_2O molecules and that, even with more H_2O molecules and a subsequently increase in hydrogen bonds, the energy still plateaued. For both Pt (011) and (111) surfaces, the overall value of E_{ads} increased somewhat as N_w increased, indicating that these two surfaces have the highest affinity for H_2O adsorption and full coverage. In this case, more water molecules will cover the surface, which could mean that a catalytic reaction, for instance, between SO_2 and H_2O could drive the reaction forward to produce more H_2 .

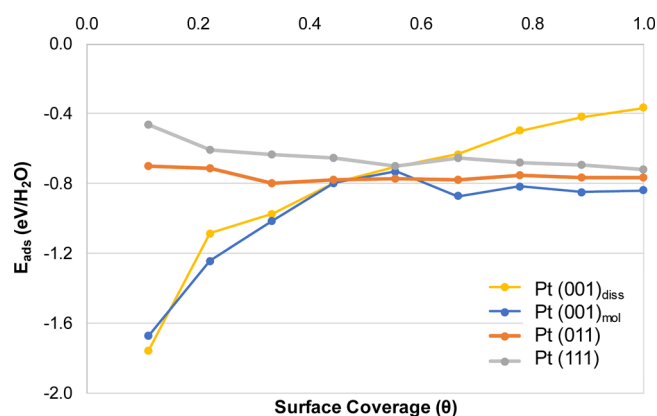


Figure 8. Average adsorption energy as a function of the H₂O coverage for the Pt (001), (011), and (111) surfaces.

Figure 9 shows the effect of H₂O coverage on the surface work function. It can be seen that the trend in the work

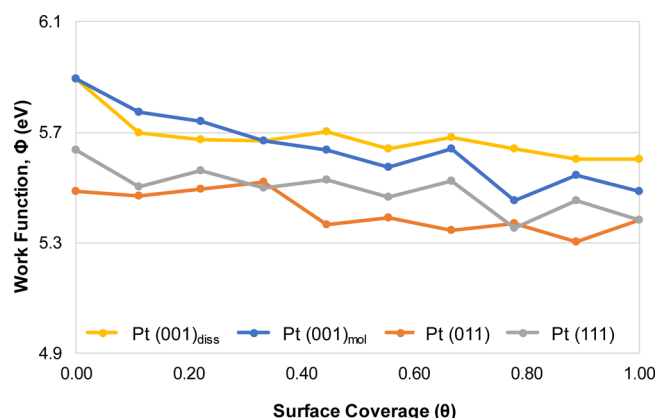


Figure 9. Work function (eV) as a function of H₂O coverage for Pt (001), (011), and (111) surfaces.

function is to decrease with increasing surface coverage for all three surfaces. As more H₂O molecules are adsorbed, more electrons are transferred to the Pt surface, leading to the reduction of the work function. Similarly to our findings, Meng and co-workers³⁴ reported that the work function decreased from 5.8 to 5.0 when the Pt (111) surface increased its H₂O coverage up to $\theta = 0.7$.

Another measure of the surface reactivity is the position of the d-band center.^{90,91} According to this model, a downward shift with respect to the Fermi level, that is, a smaller d-band center value, leads to the formation of a larger number of conduction states, which can accept electrons from the adsorbed H₂O molecules. For the pristine surfaces, the d-band center values were in the order of (111) < (001) < (011), which is in line with the surface energies. However, after adsorption of more H₂O molecules, no distinct correlation was found in this instance. Although it has been shown previously that there is a link between the electronic and electrocatalytic properties of transition metals, the relationship between the d-band center and electrocatalytic activity is more complex and does not always show a direct correlation.⁹²

To distinguish between the two competing processes, dissociation and association (i.e., molecular adsorption), and the most likely adsorption mode to occur, the thermodynamic effect of water coverage on the different Pt surfaces was

investigated. Equation 6 was used to quantify the relationship between the pressure and the chemical potential at different temperatures. In Figure 10a, we plot the H₂O pressure against

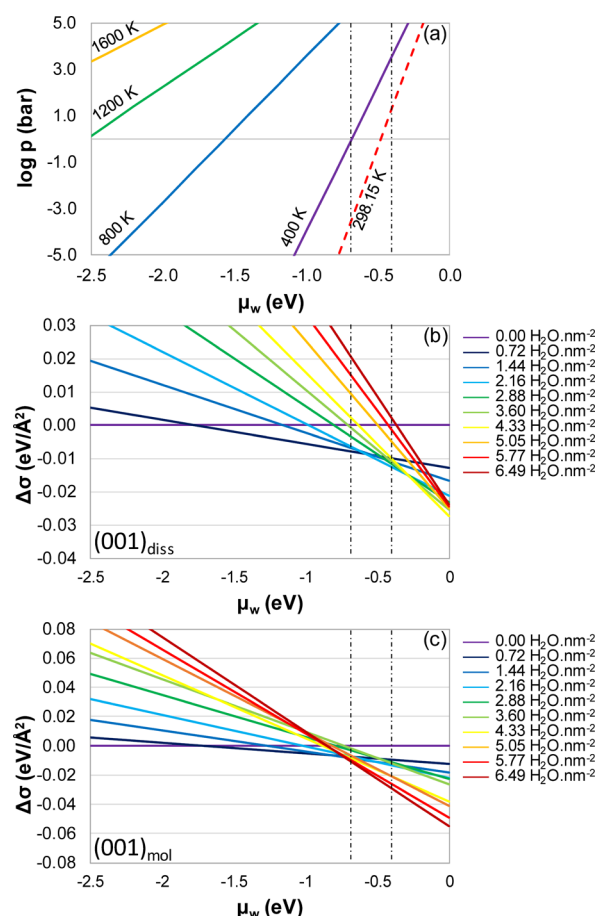


Figure 10. (a) Pressure (log P) versus chemical potential (μ_w) of H₂O at different temperatures and (b, c) effect of surface energy ($\Delta\sigma$) versus chemical potential as a function of increased coverage for the molecularly and dissociatively adsorbed H₂O molecules on the Pt (001) surface. The region between the dashed lines represents the experimental conditions for the HyS cycle (1 atm, 298–400 K).

the chemical potential at different temperatures, while in Figure 10b,c, we present the effect of the coverage on the surface free energies in terms of the chemical potential (μ_w /eV) for the dissociatively and molecularly adsorbed H₂O molecules on the Pt (001) surface. The region between the dashed lines represents the chemical potential of the experimental conditions, where the HyS cycle is operated at an ambient pressure of 1 atm and 298–400 K.

In Figure 10b, each colored line represents different coverages of the dissociated H₂O molecule on the (001) surface as a function of the surface energy and chemical potential. Overall, it was found that the pressure did not have a significant effect on the behavior of the surfaces. As the chemical potential decreases, the surface energy increases until total dehydration of the surface occurs. Under the HyS cycle reaction conditions, the (001) surface has a coverage of 2.16 H₂O·nm⁻². If the temperature decreases or pressure increases, the surface coverage decreases to 0.72 H₂O·nm⁻², but even at low temperatures, the surface does not form a monolayer of dissociated H₂O.

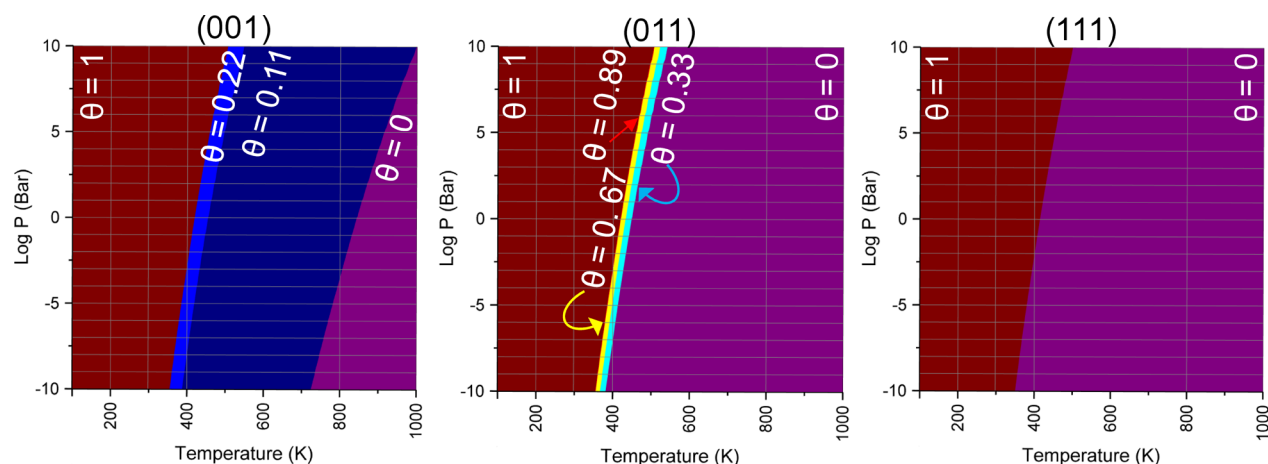


Figure 11. Surface phase diagrams in terms of pressure and temperature for molecular water adsorption at the Pt (001), (011), and (111) surfaces.

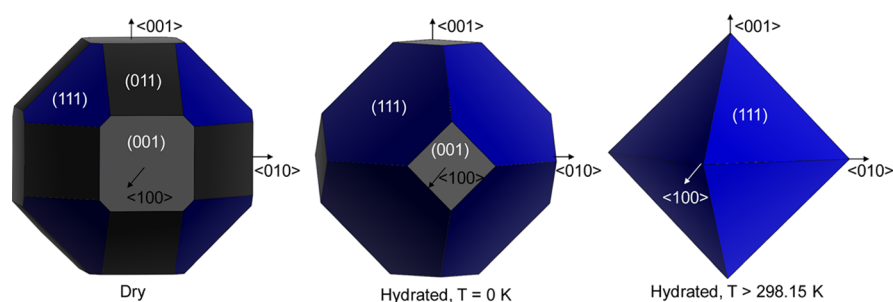


Figure 12. Wulff morphology of Pt nanoparticles: dry and hydrated at a temperature of 0 K and higher than 298.15 K.

Similarly, for the molecularly adsorbed water molecules on the Pt (001) surface (Figure 10c), we observe that, as the chemical potential decreases, the surface energy increases. In the experimental region, irrespective of temperature or pressure, the surface coverage was $6.49 \text{ H}_2\text{O} \cdot \text{nm}^{-2}$, that is, much higher coverage than for the dissociated water molecule. Molecular and ensuing dissociative water adsorptions are, to some extent, competing processes. Although we have considered the processes separately, rather than in a system containing both types of adsorption, the results shown in Figure 10b,c indicate that it is unlikely that all H_2O molecules on the (001) surface will dissociate. Although dissociation of one H_2O was favored on the (001) surface, subsequent water adsorption beyond a fairly low coverage is likely to remain bound molecularly. The chemical potential versus surface energy graphs for the (011) and (111) surfaces are displayed in the Supporting Information.

Figure 11 shows surface phase diagrams, which are constructed by considering the effect of pressure and temperature on the H_2O coverages. The (001)_{mol} system shows that, under the HyS cycle reaction (experimental) conditions, the surface will have a full coverage. The coverage changes from $\theta = 1$ to 0.22 for temperatures higher than 400 K, and we see that complete desorption occurs at temperatures higher than 850 K. The (011) surface has full coverage at low temperatures, but as the temperature increases, especially in the region between 400 and 450 K, the coverage changes from 1 to 0. In contrast to these two surfaces, the (111) surface has only two surface coverages, either fully hydrated or dry, depending on the temperature. Complete water desorption occurs around 1 atm and 425 K.

Under the HyS cycle reaction conditions, adsorption of water to full coverage will occur on all pristine Pt surfaces. However, if the temperature during an experiment were to increase above 400 K, the water will start to desorb from the surface. Further temperature increases, that is, from 450 K for (011) and (111), and 800 K for (001), will dry out the catalyst, which will make it unsuitable for the electro-oxidation of SO_2 as no H_2O will be present. This, in turn, will impact negatively on the efficiency of the HyS cycle. Comparing our results with experimental thermal desorption values, it has been reported that, even at the lowest coverages, water desorbs from the (111) surface in two peaks, 179 and 196 K, and at higher coverages, there are three distinct peaks from physisorbed water, 160–167, 170–171, and 177–180 K, ascribed to multilayer ice, a bilayer region, and a nonbilayer region, respectively.^{93,94}

If the surface energies are used to construct nanoparticle morphologies, following the Wulff construction method,⁶⁰ we can visualize the effect of the water chemical potential on the Pt nanoparticles (Figure 12). The dry morphology was constructed from the free energies of the surfaces without adsorbed H_2O molecules. The dry nanoparticle shows all three major Pt surfaces, producing a rhombicuboctahedron structure with 8 truncated triangular (111) faces, 12 truncated (011) faces, and 6 square (001) faces.

The hydrated Wulff morphologies were constructed using surface free energies, taking both the temperature and pressure of the adsorbed H_2O into account. Looking at the morphology constructed at 0 K, only the (001) and (111) surfaces are expressed. This truncated octahedron (six square and eight hexagonal faces) was also reported by Shi and Sun⁸⁵ at 0 K, where the nanoparticle expressed 86% of the (111) surface and

14% of the (110) surface. Three temperatures (298.15, 400, and 800 K) at $p_{\text{H}_2\text{O}} = 1$ atm were chosen to present the effect of temperature change on the Pt morphology. An increase in temperature changed the Pt morphology to one where only the (111) surface was expressed at all these temperatures, shown as the third octahedron morphology (eight triangular faces) in Figure 12. Zhu and co-workers⁹⁵ also utilized the DFT-GGA method to optimize varying sizes of Pt surfaces to construct Wulff morphologies and reported that the vapor pressure and temperature had a significant effect on the shape of the Pt nanoparticle. In another experimental study by Lee et al.,⁹⁶ it was seen that colloidal particles of Pt preferentially expressed the (001) and (111) facets. However, in Lee's study, all three Miller indexes were expressed to varying extent in the nanoparticles, depending on the temperature.

4. CONCLUSIONS

In this paper, we have used density functional theory calculations to predict the interaction of H_2O with the Pt (001), (011), and (111) surfaces. It was determined that the DFT-D3(BJ) dispersion method provides the best surface energies and lattice parameter when compared to experimental values. When considering adsorption of an isolated H_2O molecule, it adsorbs dissociatively on the (001) surface, whereas on both the (011) and (111) surfaces, the H_2O molecule adsorbs parallel atop the Pt atoms. Bader analysis shows that the molecularly bound H_2O provides $\sim 0.1 e^-$ to the Pt surface, while $\sim 0.4 e^-$ was transferred from the surface to the molecule when it dissociates.

Surface coverage was increased until a monolayer was obtained, where $E_{\text{ads}}/\text{H}_2\text{O}$ decreased for the (001) surface as the coverage increased, while for the (011) and (111) surfaces, $E_{\text{ads}}/\text{H}_2\text{O}$ increased. Under the conditions at which the HyS reaction takes place, the highest coverage was obtained for the (011) surface, followed by (111) and (001). The Wulff morphology of the Pt nanoparticle showed that, in a dry environment, all three surfaces are expressed. However, in a hydrated environment and with increasing temperature, the percentage of the expressed (001) and (011) faces changes until only the (111) surface is present.

Future work will include the consideration of SO_2 on various Pt surfaces, as well as a mixture of H_2O and SO_2 . In addition, we will also investigate the mechanism of the SO_2 oxidation on the Pt surfaces.

■ ASSOCIATED CONTENT

Supporting Information

The Supporting Information is available free of charge on the ACS Publications website at DOI: 10.1021/acs.jpcc.9b06136.

Graph showing the d-band center values versus H_2O coverage on the Pt (001)_{diss}, (001)_{mol}, (011) and (111) surfaces; and graph showing the effect of surface energy versus chemical potential as a function of increased coverage for Pt (011) and (111) (PDF)

■ AUTHOR INFORMATION

Corresponding Authors

*E-mail: Cornie.VanSittert@nwu.ac.za (C.G.C.E.v.S.).

*E-mail: deLeeuwN@cardiff.ac.uk (N.H.d.L.).

ORCID

Marietjie J. Ungerer: 0000-0002-9073-1186

David Santos-Carballal: 0000-0002-3199-9588

Cornelia G. C. E. van Sittert: 0000-0001-5786-5409

Nora H. de Leeuw: 0000-0002-8271-0545

Notes

The authors declare no competing financial interest.

■ ACKNOWLEDGMENTS

We acknowledge the Economic and Social Research Council (ESRC grant no. ES/N013867/1) and the Engineering and Physical Sciences Research Council (EPSRC grant nos. EP/K016288/1 and EP/K009567/2). This work was performed using the computational facilities of the Advanced Research Computing at Cardiff (ARCCA) Division, Cardiff University, and the Centre of High Performance Computing (CHPC) in Cape Town, South Africa. In addition, the calculations were carried out using the Supercomputing Facilities at Cardiff University operated by ARCCA on behalf of the HPC Wales and Supercomputing Wales (SCW) projects. We acknowledge the support of the latter, which is part-funded by the European Regional Development Fund (ERDF) via the Welsh Government. We wish to acknowledge the use of the EPSRC-funded National Chemical Database Service hosted by the Royal Society of Chemistry. D.S.-C. is grateful to the Department of Science and Technology (DST) and the National Research Foundation (NRF) of South Africa for the provision of a Postdoctoral Fellowship for Early Career Researchers from U.K. M.J.U. would like to acknowledge the National Research Foundation (NRF grant no. 116728) for their financial support and the North-West University for their support and resources. All data created during this research are openly available from Cardiff University's Research Portal at <http://dx.doi.org/10.17035/d.2019.0068143277>.

■ REFERENCES

- (1) Dai, K.; Bergot, A.; Liang, C.; Xiang, W.-N.; Huang, Z. Environmental Issues Associated with Wind Energy – A Review. *Renewable Energy* **2015**, *75*, 911–921.
- (2) Harvey, L. D. D. The Potential of Wind Energy to Largely Displace Existing Canadian Fossil Fuel and Nuclear Electricity Generation. *Energy* **2013**, *50*, 93–102.
- (3) Bahadori, A.; Nwaoha, C. A Review on Solar Energy Utilisation in Australia. *Renewable Sustainable Energy Rev.* **2013**, *18*, 1–5.
- (4) Sarver, T.; Al-Qaraghuli, A.; Kazmerski, L. L. A Comprehensive Review of the Impact of Dust on the Use of Solar Energy: History, Investigations, Results, Literature, and Mitigation Approaches. *Renewable Sustainable Energy Rev.* **2013**, *22*, 698–733.
- (5) Kaldellis, J. K. The Contribution of Small Hydro Power Stations to the Electricity Generation in Greece: Technical and Economic Considerations. *Energy Policy* **2007**, *35*, 2187–2196.
- (6) Philpott, A.; Guan, Z.; Khazaei, J.; Zakeri, G. Production Inefficiency of Electricity Markets with Hydro Generation. *Util. Policy* **2010**, *18*, 174–185.
- (7) Rehman, S.; Al-Hadhrani, L. M.; Alam, M. M. Pumped Hydro Energy Storage System: A Technological Review. *Renewable Sustainable Energy Rev.* **2015**, *44*, 586–598.
- (8) Angarita, J. L.; Usaola, J.; Martínez-Crespo, J. Combined Hydro-Wind Generation Bids in a Pool-Based Electricity Market. *Electr. Power Syst. Res.* **2009**, *79*, 1038–1046.
- (9) Suomalainen, K.; Pritchard, G.; Sharp, B.; Yuan, Z.; Zakeri, G. Correlation Analysis on Wind and Hydro Resources with Electricity Demand and Prices in New Zealand. *Appl. Energy* **2015**, *137*, 445–462.
- (10) Santos-Alamillos, F. J.; Pozo-Vázquez, D.; Ruiz-Arias, J. A.; Von Bremen, L.; Tovar-Pescador, J. Combining Wind Farms with Concentrating Solar Plants to Provide Stable Renewable Power. *Renewable Energy* **2015**, *76*, 539–550.

- (11) Ahmed, N. A.; Miyatake, M.; Al-Othman, A. K. Power Fluctuations Suppression of Stand-Alone Hybrid Generation Combining Solar Photovoltaic/Wind Turbine and Fuel Cell Systems. *Energy Convers. Manage.* **2008**, *49*, 2711–2719.
- (12) Vick, B. D.; Moss, T. A. Adding Concentrated Solar Power Plants to Wind Farms to Achieve a Good Utility Electrical Load Match. *Sol. Energy* **2013**, *92*, 298–312.
- (13) Colón-Mercado, H. R.; Hobbs, D. T. Catalyst Evaluation for a Sulfur Dioxide-Depolarized Electrolyzer. *Electrochem. Commun.* **2007**, *9*, 2649–2653.
- (14) de Bruijn, F. The Current Status of Fuel Cell Technology for Mobile and Stationary Applications. *Green Chem.* **2005**, *7*, 132–150.
- (15) Cormos, C.-C. Hydrogen Production from Fossil Fuels with Carbon Capture and Storage Based on Chemical Looping Systems. *Int. J. Hydrogen Energy* **2011**, *36*, 5960–5971.
- (16) Ni, M.; Leung, D. Y. C.; Leung, M. K. H.; Sumathy, K. An Overview of Hydrogen Production from Biomass. *Fuel Process. Technol.* **2006**, *87*, 461–472.
- (17) Acar, C.; Dincer, I.; Naterer, G. F. Review of Photocatalytic Water-Splitting Methods for Sustainable Hydrogen Production. *Int. J. Energy Res.* **2016**, *40*, 1449–1473.
- (18) Ursua, A.; Gandía, L. M.; Sanchis, P. Hydrogen Production From Water Electrolysis: Current Status and Future Trends. *Proc. IEEE* **2012**, *100*, 410–426.
- (19) Xue, L.; Zhang, P.; Chen, S.; Wang, L. Pt-Based Bimetallic Catalysts for SO₂-Depolarized Electrolysis Reaction in the Hybrid Sulfur Process. *Int. J. Hydrogen Energy* **2014**, *39*, 14196–14203.
- (20) O'Brien, J. A.; Hinkley, J. T.; Donne, S. W.; Lindquist, S. E. The Electrochemical Oxidation of Aqueous Sulfur Dioxide: A Critical Review of Work with Respect to the Hybrid Sulfur Cycle. *Electrochim. Acta* **2010**, *55*, 573–591.
- (21) Appleby, A.; Pinchon, B. Electrochemical Aspects of the H₂SO₄–SO₂ Thermoelectrochemical Cycle for Hydrogen Production. *Int. J. Hydrogen Energy* **1980**, *5*, 253–267.
- (22) Lu, P. W. T.; Ammon, R. L. An Investigation of Electrode Materials for the Anodic Oxidation of Sulfur Dioxide in Concentrated Sulfuric Acid. *J. Electrochem. Soc.* **1980**, *127*, 2610.
- (23) Sui, S.; Wang, X.; Zhou, X.; Su, Y.; Riffat, S.; Liu, C. A Comprehensive Review of Pt Electrocatalysts for the Oxygen Reduction Reaction: Nanostructure, Activity, Mechanism and Carbon Support in PEM Fuel Cells. *J. Mater. Chem. A* **2017**, *5*, 1808–1825.
- (24) Luo, H.; Park, S.; Chan, H. Y. H.; Weaver, M. J. Surface Oxidation of Platinum-Group Transition Metals in Ambient Gaseous Environments: Role of Electrochemical versus Chemical Pathways. *J. Phys. Chem. B* **2000**, *104*, 8250–8258.
- (25) Brini, E.; Fennell, C. J.; Fernandez-Serra, M.; Hribar-Lee, B.; Lukšič, M.; Dill, K. A. How Water's Properties Are Encoded in Its Molecular Structure and Energies. *Chem. Rev.* **2017**, *117*, 12385–12414.
- (26) Björneholm, O.; Hansen, M. H.; Hodgson, A.; Liu, L. M.; Limmer, D. T.; Michaelides, A.; Pedevilla, P.; Rossmels, J.; Shen, H.; Tocci, G.; et al. Water at Interfaces. *Chem. Rev.* **2016**, *116*, 7698–7726.
- (27) Schnur, S.; Groß, A. Properties of Metal–Water Interfaces Studied from First Principles. *New J. Phys.* **2009**, *11*, 125003.
- (28) Forster-Tonigold, K.; Groß, A. Dispersion Corrected RPBE Studies of Liquid Water. *J. Chem. Phys.* **2014**, *141*, 064501.
- (29) Klimeš, J.; Bowler, D. R.; Michaelides, A. Chemical Accuracy for the van Der Waals Density Functional. *J. Phys. Condens. Matter* **2010**, *22*, 022201.
- (30) Carrasco, J.; Klimeš, J.; Michaelides, A. The Role of van Der Waals Forces in Water Adsorption on Metals. *J. Chem. Phys.* **2013**, *138*, No. 024708.
- (31) Tkatchenko, A.; Scheffler, M. Accurate Molecular Van Der Waals Interactions from Ground-State Electron Density and Free-Atom Reference Data. *Phys. Rev. Lett.* **2009**, *102*, No. 073005.
- (32) Bellarosa, L.; García-Muelas, R.; Revilla-López, G.; López, N. Diversity at the Water-Metal Interface: Metal, Water Thickness, and Confinement Effects. *ACS Cent. Sci.* **2016**, *2*, 109–116.
- (33) Carrasco, J.; Hodgson, A.; Michaelides, A. A Molecular Perspective of Water at Metal Interfaces. *Nat. Mater.* **2012**, *11*, 667–674.
- (34) Meng, S.; Wang, E. G.; Gao, S. Water Adsorption on Metal Surfaces: A General Picture from Density Functional Theory Studies. *Phys. Rev. B* **2004**, *69*, 195404.
- (35) Kenmoe, S.; Biedermann, P. U. Water Aggregation and Dissociation on the ZnO(10 $\bar{1}$ 0) Surface. *Phys. Chem. Chem. Phys.* **2017**, *19*, 1466–1486.
- (36) Kresse, G.; Hafner, J. Ab Initio Molecular Dynamics for Liquid Metals. *Phys. Rev. B* **1993**, *47*, 558–561.
- (37) Kresse, G.; Hafner, J. Ab Initio Molecular-Dynamics Simulation of the liquid-metal–amorphous-semiconductor Transition in Germanium. *Phys. Rev. B* **1994**, *49*, 14251–14269.
- (38) Kresse, G.; Furthmüller, J. Efficient Iterative Schemes for Ab Initio Total-Energy Calculations Using a Plane-Wave Basis Set. *Phys. Rev. B* **1996**, *54*, 11169–11186.
- (39) Kresse, G.; Furthmüller, J. Efficiency of Ab-Initio Total Energy Calculations for Metals and Semiconductors Using a Plane-Wave Basis Set. *Comput. Mater. Sci.* **1996**, *6*, 15–50.
- (40) Blöchl, P. E. Projector Augmented-Wave Method. *Phys. Rev. B* **1994**, *50*, 17953–17979.
- (41) Kresse, G.; Joubert, D. From ultrasoft pseudopotentials to the projector augmented-wave method. *Phys. Rev. B* **1999**, *59*, 1758–1775.
- (42) Perdew, J. P.; Burke, K.; Ernzerhof, M. Generalized Gradient Approximation Made Simple. *Phys. Rev. Lett.* **1996**, *77*, 3865–3868.
- (43) Perdew, J. P.; Burke, K.; Ernzerhof, M. Generalized Gradient Approximation Made Simple [Phys. Rev. Lett. **77**, 3865 (1996)]. *Phys. Rev. Lett.* **1997**, *78*, 1396.
- (44) Grimme, S.; Ehrlich, S.; Goerigk, L. Effect of the Damping Function in Dispersion Corrected Density Functional Theory. *J. Comput. Chem.* **2011**, *32*, 1456–1465.
- (45) Methfessel, M.; Paxton, A. T. High-Precision Sampling for Brillouin-Zone Integration in Metals. *Phys. Rev. B* **1989**, *40*, 3616–3621.
- (46) Blöchl, P. E.; Jepsen, O.; Andersen, O. K. Improved Tetrahedron Method for Brillouin-Zone Integrations. *Phys. Rev. B* **1994**, *49*, 16223–16233.
- (47) Corbel, G.; Topić, M.; Gibaud, A.; Lang, C. I. Selective Dry Oxidation of the Ordered Pt-11.1 at.% v Alloy Surface Evidenced by in Situ Temperature-Controlled X-Ray Diffraction. *J. Alloys Compd.* **2011**, *509*, 6532–6538.
- (48) Monkhorst, H. J.; Pack, J. D. Special Points for Brillouin-zone Integrations. *Phys. Rev. B* **1976**, *13*, 5188–5192.
- (49) Arblaster, J. W. Crystallographic Properties of Platinum. *Platinum Met. Rev.* **1997**, *41*, 12–21.
- (50) Arblaster, J. W. Crystallographic Properties of Platinum: New Methodology and Erratum. *Platinum Met. Rev.* **2006**, *50*, 118–119.
- (51) Watson, G. W.; Kelsey, E. T.; de Leeuw, N. H.; Harris, D. J.; Parker, S. C. Atomistic Simulation of Dislocations, Surfaces and Interfaces in MgO. *J. Chem. Soc., Faraday Trans.* **1996**, *92*, 433.
- (52) Henkelman, G.; Arnaldsson, A.; Jónsson, H. A Fast and Robust Algorithm for Bader Decomposition of Charge Density. *Comput. Mater. Sci.* **2006**, *36*, 354–360.
- (53) Sanville, E.; Kenny, S. D.; Smith, R.; Henkelman, G. Improved Grid-Based Algorithm for Bader Charge Allocation. *J. Comput. Chem.* **2007**, *28*, 899–908.
- (54) Tang, W.; Sanville, E.; Henkelman, G. A Grid-Based Bader Analysis Algorithm without Lattice Bias. *J. Phys. Condens. Matter* **2009**, *21*, No. 084204.
- (55) Yu, M.; Trinkle, D. R. Accurate and Efficient Algorithm for Bader Charge Integration. *J. Chem. Phys.* **2011**, *134*, No. 064111.
- (56) Tersoff, J.; Hamann, D. R. Theory of the Scanning Tunneling Microscope. *Phys. Rev. B* **1985**, *31*, 805–813.
- (57) Vanpoucke, D. E. P.; Brocks, G. Pt-Induced Nanowires on Ge(001): A Density Functional Theory Study. *Phys. Rev. B* **2010**, *81*, No. 085410.

- (58) Santos-Carballal, D.; Roldan, A.; Grau-Crespo, R.; de Leeuw, N. H. A DFT Study of the Structures, Stabilities and Redox Behaviour of the Major Surfaces of Magnetite Fe_3O_4 . *Phys. Chem. Chem. Phys.* **2014**, *16*, 21082–21097.
- (59) Chase, M. W. *NIST-JANAF Thermochemical Tables*; 4th edition; American Institute of Physics, 1998; Vol. Monograph.
- (60) Wulff, G. XXV. Zur Frage Der Geschwindigkeit Des Wachstums Und Der Auflösung Der Krystallflächen. *Z. Kristallogr. Cryst. Mater.* **1901**, *34*, 449–530.
- (61) Fleming, S.; Rohl, A. GDIS: A visualization Program for Molecular and Periodic Systems. *Z. Kristallogr. Cryst. Mater.* **2005**, *220*, 580–584.
- (62) Posada-Pérez, S.; Santos-Carballal, D.; Terranova, U.; Roldan, A.; Illas, F.; de Leeuw, N. H. CO_2 interaction with Violarite (FeNi_2S_4) Surfaces: A Dispersion-Corrected DFT Study. *Phys. Chem. Chem. Phys.* **2018**, *20*, 20439–20446.
- (63) Grimme, S. Semiempirical GGA-Type Density Functional Constructed with a Long-Range Dispersion Correction. *J. Comput. Chem.* **2006**, *27*, 1787–1799.
- (64) Grimme, S.; Antony, J.; Ehrlich, S.; Krieg, H. A Consistent and Accurate Ab Initio Parametrization of Density Functional Dispersion Correction (DFT-D) for the 94 Elements H–Pu. *J. Chem. Phys.* **2010**, *132*, 154104.
- (65) Getman, R. B.; Xu, Y.; Schneider, W. F. Thermodynamics of Environment-Dependent Oxygen Chemisorption on Pt(111). *J. Phys. Chem. C* **2008**, *112*, 9559–9572.
- (66) Skriver, H. L.; Rosengaard, N. M. Surface Energy and Work Function of Elemental Metals. *Phys. Rev. B* **1992**, *46*, 7157–7168.
- (67) Santos-Carballal, D.; Ngoepe, P. E.; de Leeuw, N. H. Ab Initio Investigation of the Thermodynamics of Cation Distribution and of the Electronic and Magnetic Structures in the LiMn_2O_4 Spinel. *Phys. Rev. B* **2018**, *97*, 085126.
- (68) Klimeš, J.; Bowler, D. R.; Michaelides, A. Van Der Waals Density Functionals Applied to Solids. *Phys. Rev. B* **2011**, *83*, 195131.
- (69) Jian-Min, Z.; Fei, M.; Ke-Wei, X. Calculation of the Surface Energy of Fcc Metals with Modified Embedded-Atom Method. *Chin. Phys.* **2004**, *13*, 1082–1090.
- (70) Singh-Miller, N. E.; Marzari, N. Surface Energies, Work Functions, and Surface Relaxations of Low-Index Metallic Surfaces from First Principles. *Phys. Rev. B* **2009**, *80*, 235407.
- (71) Keene, B. J. Review of Data for the Surface Tension of Pure Metals. *Int. Mater. Rev.* **2013**, *38*, 157–192.
- (72) Tyson, W. R.; Miller, W. A. Surface Free Energies of Solid Metals: Estimation from Liquid Surface Tension Measurements. *Surf. Sci.* **1977**, *62*, 267–276.
- (73) Xin, H.; Linic, S. Communications: Exceptions to the d-Band Model of Chemisorption on Metal Surfaces: The Dominant Role of Repulsion between Adsorbate States and Metal d-States. *J. Chem. Phys.* **2010**, *132*, 221101.
- (74) Caglar, B.; Kizilkaya, A. C.; Niemantsverdriet, J. W.; Weststrate, C. J. Application of Work Function Measurements in the Study of Surface Catalyzed Reactions on Rh(1 0 0). *Catal., Struct. React.* **2018**, *4*, 1–11.
- (75) Norskov, J. K.; Abild-Pedersen, F.; Studt, F.; Bligaard, T. Density Functional Theory in Surface Chemistry and Catalysis. *Proc. Natl. Acad. Sci.* **2011**, *108*, 937–943.
- (76) Walen, H.; Liu, D.-J.; Oh, J.; Yang, H. J.; Spurgeon, P. M.; Kim, Y.; Thiel, P. A. Sulfur Atoms Adsorbed on Cu(100) at Low Coverage: Characterization and Stability against Complexation. *J. Phys. Chem. B* **2017**, *122*, 963–971.
- (77) Andryushechkin, B. V.; Zhidomirov, G. M.; Eltsov, K. N.; Hladchanka, Y. V.; Korlyukov, A. A. Local Structure of the Ag(100) Surface Reacting with Molecular Iodine: Experimental and Theoretical Study. *Phys. Rev. B* **2009**, *80*, 125409.
- (78) Feenstra, R. M.; Hla, S. W. Introduction to Scanning Tunneling Microscopy of Metals and Semiconductor. In *Physics of Solid Surfaces*; Springer: 2015; pp 15.
- (79) Lee, S.; Park, J.; Ragan, R.; Kim, S.; Lee, Z.; Lim, D. K.; Ohlberg, D. A. A.; Williams, R. S. Self-Assembled Monolayers on Pt(111): Molecular Packing Structure and Strain Effects Observed by Scanning Tunneling Microscopy. *J. Am. Chem. Soc.* **2006**, *128*, 5745–5750.
- (80) Ludwig, R. How Does Water Bind to Metal Surfaces: Hydrogen Atoms Up or Hydrogen Atoms Down? *Angew. Chem., Int. Ed.* **2003**, *42*, 3458–3460.
- (81) Benedict, W. S.; Gailar, N.; Plyler, E. K. Rotation-Vibration Spectra of Deuterated Water Vapor. *J. Chem. Phys.* **1956**, *24*, 1139–1165.
- (82) Thiel, P. A.; Madey, T. E. The Interaction of Water with Solid Surfaces: Fundamental Aspects. *Surf. Sci. Rep.* **1987**, *7*, 211–385.
- (83) Henderson, M. The Interaction of Water with Solid Surfaces: Fundamental Aspects Revisited. *Surf. Sci. Rep.* **2002**, *46*, 1–308.
- (84) Feibelman, P. J. Partial Dissociation of Water on Ru(0001). *Science* **2002**, *295*, 99–102.
- (85) Shi, Q.; Sun, R. Adsorption Manners of Hydrogen on Pt(1 0 0), (1 1 0) and (1 1 1) Surfaces at High Coverage. *Comput. Theor. Chem.* **2017**, *1106*, 43–49.
- (86) Iwasita, T.; Xia, X. Adsorption of Water at Pt(111) Electrode in HClO_4 Solutions. The Potential of Zero Charge. *J. Electroanal. Chem.* **1996**, *411*, 95–102.
- (87) Mohamed, F.; VandeVondele, J.; Hutter, J.; Krack, M.; Parrinello, M.; Chassaing, T. Quickstep: Fast and Accurate Density Functional Calculations Using a Mixed Gaussian and Plane Waves Approach. *Comput. Phys. Commun.* **2005**, *167*, 103–128.
- (88) Feibelman, P. J.; Bartelt, N. C.; Nie, S.; Thürmer, K. Interpretation of High-Resolution Images of the Best-Bound Wetting Layers on Pt(111). *J. Chem. Phys.* **2010**, *133*, 154703.
- (89) Standop, S.; Redinger, A.; Morgenstern, M.; Michely, T.; Busse, C. Molecular Structure of the H_2O Wetting Layer on Pt(111). *Phys. Rev. B* **2010**, *82*, 161412.
- (90) Hammer, B.; Norskov, J. K. Electronic Factors Determining the Reactivity of Metal Surfaces. *Surf. Sci.* **1995**, *343*, 211–220.
- (91) Hammer, B.; Norskov, J. K. Why Gold Is the Noblest of All the Metals. *Nature* **1995**, *376*, 238–240.
- (92) Gorzkowski, M. T.; Lewera, A. Probing the Limits of D-Band Center Theory: Electronic and Electrocatalytic Properties of Pd-Shell–Pt-Core Nanoparticles. *J. Phys. Chem. C* **2015**, *119*, 18389–18395.
- (93) Fisher, G. B.; Gland, J. L. The Interaction of Water with the Pt(111) Surface. *Surf. Sci.* **1980**, *94*, 446–455.
- (94) Jo, S. K.; Kiss, J.; Polanco, J. A.; White, J. M. Identification of Second Layer Adsorbates: Water and Chloroethane on Pt(111). *Surf. Sci.* **1991**, *253*, 233–244.
- (95) Zhu, B.; Xu, Z.; Wang, C.; Gao, Y. Shape Evolution of Metal Nanoparticles in Water Vapor Environment. *Nano Lett.* **2016**, *16*, 2628–2632.
- (96) Lee, I.; Morales, R.; Albitzer, M. A.; Zaera, F. Synthesis of Heterogeneous Catalysts with Well Shaped Platinum Particles to Control Reaction Selectivity. *Proc. Natl. Acad. Sci.* **2008**, *105*, 15241–15246.